



Article

Highly Selective NH₃ Sensor Based on MoS₂/WS₂ Heterojunction

Min Zhang ^{1,2,*} and Jinzhu Zhang ^{1,2}

¹ Xinjiang Key Laboratory of Solid State Physics and Devices, Xinjiang University, Urumqi 830046, China; 18894001858@163.com

² School of Physics Science and Technology, Xinjiang University, Urumqi 830046, China

* Correspondence: minzhang0816@163.com

Abstract: In this paper, the heterostructure of MoS₂/WS₂ was prepared by a hydrothermal method; the n-n heterostructure was demonstrated using TEM combined with Mott-Schottky analysis. The valence and conduction band positions were further identified by the XPS valence band spectra. The NH₃-sensing properties were assessed at room temperature by changing the mass ratio of the MoS₂ and WS₂ components. The 50 wt%-MoS₂/WS₂ sample exhibited the best performance, with a peak response of 23643% to NH₃ at a concentration of 500 ppm, a minimum detection limit of 20 ppm, and a fast recovery time of 2.6 s. Furthermore, the composites-based sensors demonstrated an excellent humidity immune property with less than one order of magnitude in the humidity range of 11–95% RH, revealing the practical application value of these sensors. These results suggest that the MoS₂/WS₂ heterojunction is an intriguing candidate for fabricating NH₃ sensors.

Keywords: MoS₂/WS₂; anti-humidity; ammonia sensing properties; heterojunction

1. Introduction

Ammonia (NH₃) is a colorless and strongly irritating odor gas that is among the most prevalent indoor pollutant gases that is lighter than air (specific gravity of 0.5), with a minimum perceptible concentration of 30 ppm [1]. The solubility of ammonia is so high that it has an irritating and corrosive effect, particularly on the upper respiratory tracts of animals or humans. Humans' respiratory, pulmonary, and immune systems suffer severe damage when exposed to environments with NH₃ concentrations above 50 ppm for more than 30 min [2,3]. Therefore, it is critical to effectively monitor low-concentration NH₃ in real time.

When compared to semiconductor gas sensors, the methods typically employed for detecting gases are spectrophotometric [4], gas chromatography [5], and electrochemical sensors [6], but these have specific limitations, such as complicated operation, high costs, and inability to monitor in real-time, thereby restricting their practical applications. Semiconductor gas sensors are widely used in environmental monitoring and security systems due to their portability, simplicity of operation, and low detection costs [7,8].

Tungsten disulfide (WS₂), a typical n-type semiconducting material, has been utilized in light-emitting diodes, energy storage devices, and semiconductor gas sensors [9,10]. WS₂ with two-dimensional morphology generally exhibits a large specific surface area, high electron mobility, and excellent thermal stability. Shivani Sharma [11], and Xu [12] et al. reported that WS₂ nanosheet-based ammonia (NH₃) sensors exhibited an excellent performance. Li et al. [13] employed commercially available WS₂ powder to construct a WS₂ nanosheet-based NH₃ sensor with a long response time. However, the response towards NH₃ increased as the ambient humidity increased. The WS₂ nanosheets were unstable due to the adsorption of water molecules in the air, and also their sensitivity to NH₃ was deemed to be too low for practical applications [14–20]. Researchers have explored that the primary cause of this instability is weak van der Waals force interactions



Citation: Zhang, M.; Zhang, J. Highly Selective NH₃ Sensor Based on MoS₂/WS₂ Heterojunction.

Nanomaterials **2023**, *13*, 1835. <https://doi.org/10.3390/nano13121835>

Academic Editors: Antonios Kelarakis and Jakob Birkedal Wagner

Received: 24 April 2023

Revised: 26 May 2023

Accepted: 5 June 2023

Published: 10 June 2023



Copyright: © 2023 by the authors. Licensee MDPI, Basel, Switzerland. This article is an open access article distributed under the terms and conditions of the Creative Commons Attribution (CC BY) license (<https://creativecommons.org/licenses/by/4.0/>).

between the adjacent planes in WS_2 , which enable gas molecules to freely permeate and diffuse between the layers and ultimately cause changes in the conductivity of the WS_2 material, which in turn induces the unstable gas-sensitive performance of gas sensors made from a pristine WS_2 [21,22].

As a typical two-dimensional transition metal sulfide (TMD) material, MoS_2 has been widely used in electrodes, energy storage devices, and catalysis [23–25]. Two-dimensional MoS_2 is a direct bandgap semiconductor with an optical band gap of 1.8 eV [26], and both MoS_2 and WS_2 are common 2D TMD materials with excellent stability. It has previously been reported in the literature that compositing MoS_2 with WS_2 improves the unstable properties of WS_2 as a sensitive substrate while also providing a high sensitivity. Their composites would integrate the benefits of both components and possess superior properties to any single one by producing a heterostructure between WS_2 and MoS_2 [27]. The high separation and transfer efficiency of carriers induced by the heterojunction is of great significance to the high response speed of the sensors.

In this study, we developed an NH_3 sensor based on MoS_2/WS_2 heterostructures, which was previously demonstrated theoretically. The introduction of such heterostructures increase the baseline resistance of sensors, thus improving the sensing response at room temperature, which is of great significance for the real-time monitoring of ammonia gas. Then, the response behavior of MoS_2/WS_2 to NH_3 was systematically investigated. As predicted, the gas sensor based on the MoS_2/WS_2 heterostructure exhibited an enhanced NH_3 -sensing performance, significantly lower detection limits, fast recovery, reliable resistance to moisture interference, and excellent stability. Thus, this work provides a practical approach for developing high-performance NH_3 gas sensors at room temperature.

2. Materials and Methods

2.1. Materials

Thioacetamide (C_2H_5NS), thiourea (CH_4N_2S), tungsten chloride (WCl_6), and sodium molybdate ($Na_2MoO_4 \cdot 2H_2O$) were all purchased from Shanghai Maclean, Shanghai, China. Standard gases, $HCHO$, C_2H_6O , C_3H_6O , H_2O_2 , and NH_3 were purchased from Aladdin, Seattle, WA, USA. All reagents used in the experiments were of analytical grade.

2.2. Preparation of WS_2

WS_2 nanosheets were synthesized by a hydrothermal method. A total of 5 mmol of WCl_6 and 25 mmol of C_2H_5NS were dissolved in 30 mL of deionized water, stirred magnetically for 1 h, transferred to a 50 mL autoclave, and kept at 160 °C for 10 h. The residuals were washed and centrifuged 3–5 times with deionized water and ethanol until a neutral pH was obtained and treated with ultrasound for 15 min. Finally, the products were treated in a vacuum drying oven at 60 °C for 24 h.

2.3. Preparation of MoS_2

A total of 2.5 mmol of CH_4N_2S and 0.545 mmol of $Na_2MoO_4 \cdot 2H_2O$ were weighed and mixed with 70 mL of deionized water. After that, the mixture was completely dissolved by magnetic stirring, transferred to an autoclave lined with PTFE and placed in a constant temperature oven at 200 °C for 12 h. Then, it was removed and cooled naturally. The reaction products were washed with deionized ethanol and water alternately, centrifuged, and dried at 70 °C for 10 h. Finally, MoS_2 powders were obtained.

2.4. Preparation of MoS_2/WS_2 Composites

The obtained MoS_2 and WS_2 samples were mixed at 30 wt%: 70 wt%, 50 wt%: 50 wt%, and 70 wt%: 30 wt%, respectively, with 50 mL of deionized water, and these solutions were added to an autoclave lined with PTFE. The autoclave was kept at 200 °C for 10 h, cooled to room temperature, and washed several times with ethanol and water.

Finally, it was vacuum dried at 60 °C for 10 h to obtain MoS₂/WS₂ nanocomposites containing different relative mass ratios, which were later named as 3 MW, 5 MW, and 7 MW, respectively.

2.5. Characterization

The crystal structure of the prepared sensing materials was analyzed using X-ray diffraction (XRD, D8 Advance, Cu-K α) at an operating voltage of 60 kV. To assess the Raman spectra of the prepared samples in the range of 200–700 cm⁻¹, a Raman microscope with a 532 nm laser source was used. The band-gap of the samples was tested using a UV-visible spectrophotometer (UV-visible spectrophotometer, Lambda 650, PerkinElmer, Waltham, MA, USA). X-ray photoelectron spectroscopy (XPS) analysis was performed using a ThermoEscalab 250 (Thermo Fisher Scientific, Waltham, MA, USA) equipped with a monochromatic Al K α source ($h\nu = 1486.6$ eV) to collect the formation of surface elemental assemblages and elemental states. The morphology and elements of the products were observed using a field emission scanning electron microscope (SEM, Apreo S, FEI, Hillsboro, OR, USA) equipped with an energy-dispersive X-ray spectrometer (EDX, Bruker, German). The internal microstructure of the material was observed with high resolution transmission electron microscopy (HR-TEM, FEI-Tecna G2T20, FEI Company, Hillsboro, OR, USA). The surface functional groups of the samples were evaluated using FTIR spectroscopy (Bruker, Billerica, MA, USA) in the wavelength range of 500–4000 cm⁻¹. The capacitance-voltage (C-V) relationship curves of the samples were measured with an electrochemical workstation (CHI660E model) and valence band XPS tests were performed using a Thermo Scientific ESCALAB Xi⁺ multifunctional electron spectrometer.

2.6. Gas Detection

First, the prepared WS₂, MoS₂ and MoS₂/WS₂ samples were placed in a mortar and then a small amount of deionized water was added and ground for 3 min. The Ag-Pd electrode with the ceramic substrate was then adopted, being 13.4 mm long and 7 mm wide, with a minimum width and spacing of 0.2 mm. After grinding, they were pasted on the Ag-Pd electrode sheet with a small brush and dried in a vacuum drying oven at 50 °C for 10 h. After drying, the gas-sensitive characteristics of all the samples were tested at 1 V using a comprehensive photoelectric test bench (CGS-MT). The level of the sensing response of the sensor is determined by the relative value of the current change in gas and in air, i.e., $R = (I - I_0)/I_0$, where I_0 is the current of the device in the air, and I is the current in the gas atmosphere to be measured. When the device is transferred from air to the gas to be detected, the time required for the current to reach a steady state is the response time, and when the device is removed from the gas to the air, the time required for the current to reach a steady state is determined as the recovery time.

2.7. Moisture Resistance Measurement

In moisture resistance testing, different relative humidity environments are obtained by formulating different saturated salt solutions. Different humidity levels (11–95% RH) were obtained by preparing LiCl, MgCl₂, K₂CO₃, Mg(NO₃)₂, CuCl₂, NaCl, KCl, and KNO₃ saturated salt solutions with the relative humidity of 11%, 33%, 43%, 54%, 64%, 75%, 85%, and 95%, respectively. The air humidity was 30%RH at the time of testing, with the test voltage set at AC 1 V, and a frequency of 100 Hz, respectively. The device was sequentially placed into chambers of different relative humidity for 6 min to obtain the resistance response. The manufacturing process and testing process of the WS₂/MoS₂ sensor was shown in Figure 1.

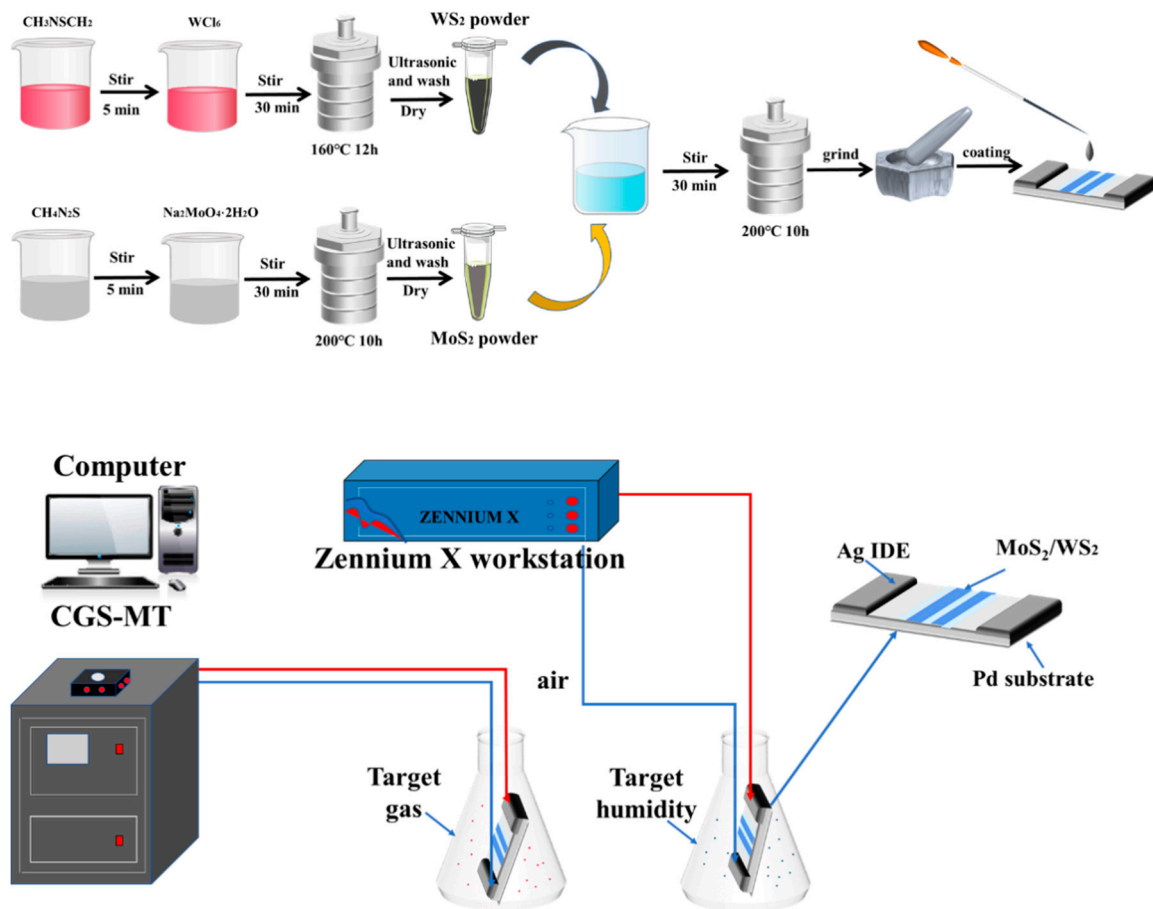


Figure 1. The manufacturing process and testing process of the WS₂/MoS₂ sensor.

3. Results

Figure 2a,b illustrates the XRD analysis of the crystal structures of WS₂ and MoS₂, where 2θ is the diffraction angle. The spectrum of WS₂ exhibits more distinct characteristic peaks at approximately 14.44° (002), 32.77° (100), 33.58° (101), 43.90° (103), and 58.42° (110), respectively, indicating that the WS₂ sample belongs to 2H-WS₂ (JCPDS:08-0237) [28]. The wide full width at half maxima and the weak peak intensity of WS₂ implies the poor crystallinity of the sample. MoS₂ peaks were located at 59.4° for the (110) plane, 32.7° for the (100) plane, and 14.44° for the (002) plane, respectively, corresponding to the 2H phase MoS₂ (JCPDS:37-1492) [29] with good crystallinity. Furthermore, the MoS₂/WS₂ composites were analyzed through XRD analysis. In the composite samples, three distinct peaks were observed; the diffraction peak of the (002) (100) (110) crystal planes originated from MoS₂, and (101) (103) (110) from WS₂, respectively. This analysis demonstrated that the phase composition of the composite samples is a mixture of WS₂ and MoS₂ [30]. It has been observed that the peaks of the (002) crystal plane in the MoS₂/WS₂ composites exhibited a high intensity. The diffraction peak intensity of the composites gradually increased as the MoS₂ composition increased, and the full width at half maxima narrowed, indicating that crystallinity improved as the relative concentration of MoS₂ in the composites increased. At the same time, no other impurity peaks were detected in the XRD patterns, revealing that WS₂ and MoS₂ are chemically compatible [31].

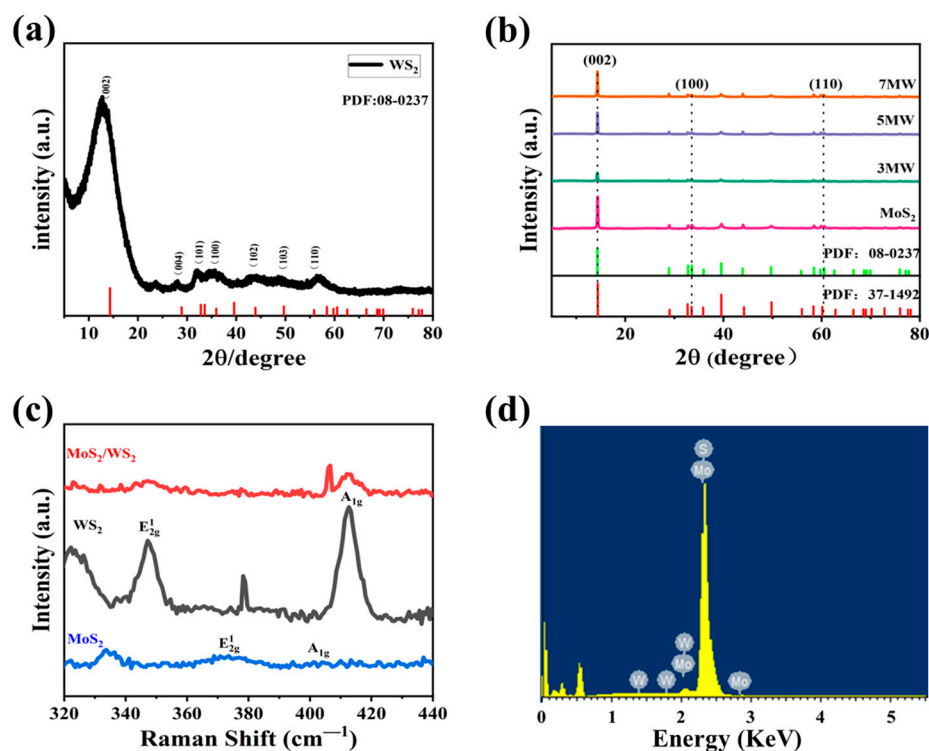


Figure 2. (a,b) The XRD patterns of the prepared WS₂, MoS₂, and MoS₂ /WS₂ composites. (c) The Raman spectra of WS₂, MoS₂, and 5 MW. (d) The corresponding energy dispersive X-ray spectrum (EDS) of the 5 MW sample.

Figure 2c depicts the Raman spectra of WS₂, MoS₂, and 5 MW samples. Both WS₂ and MoS₂ have a hexagonal structure [32], and two main Raman resonance modes: E_{2g}¹ (in-plane phonons) and A_{1g} (out-of-plane phonons). The resonance signals at 350.4, and 418.8 cm⁻¹ in WS₂ correspond to the E_{2g}¹ and A_{1g} modes, whereas the signals at 376.6 cm⁻¹ and 404.8 cm⁻¹ in MoS₂ correspond to the E_{2g}¹ and A_{1g} modes, respectively. The XRD analysis and Raman spectra of the WS₂ and MoS₂ resonance signals confirmed the successful synthesis of the MoS₂/WS₂ composites [33]. The energy dispersive spectral analysis of the 5 MW sample depicted in Figure 2d reveals the presence of the elements S, Mo, and W.

The surface composition and chemical state of the MoS₂/WS₂ composite were determined using XPS analysis, and the results are shown in Figure 3. We used the C 1s peak of 284.8 eV as a reference for the binding energy. The characteristic peaks of S 2p, Mo 3d, Mo 3p, and W 4f were observed in the MoS₂/WS₂ composites from the broad scan spectrum (Figure 3a). High-resolution XPS spectra were employed to scan the orbital peaks of Mo 3d, W 4f, and S 2p, as demonstrated in Figure 3b–d. The S 2p_{3/2} and S 2p_{1/2} states in Figure 3b appeared at 162.8 and 164.2 eV binding energy, respectively. The Mo 3d_{5/2} and Mo 3d_{3/2} peaks in Figure 3c are located at 229.9 and 233 eV, respectively, and are attributed to the Mo⁴⁺ in MoS₂ [34]. In addition, there was no Mo⁶⁺3d_{3/2} orbital peak at 236 eV in this spectra, indicating that the Mo element was not oxidized, but was converted to complete sulfide [35,36]. The W 4f spectrum in Figure 3d contains W 4f_{7/2}, W 4f_{5/2}, and W 5p_{3/2} peaks with binding energies at 33.4, 35.5, and 39.6 eV, respectively [37]. Colors that appearing in subfigures b–d are just to differentiate different fit peaks. The aforementioned results indicate that the 5 MW composite comprises the elements Mo, W, and S, implying the successful formation of this composite.

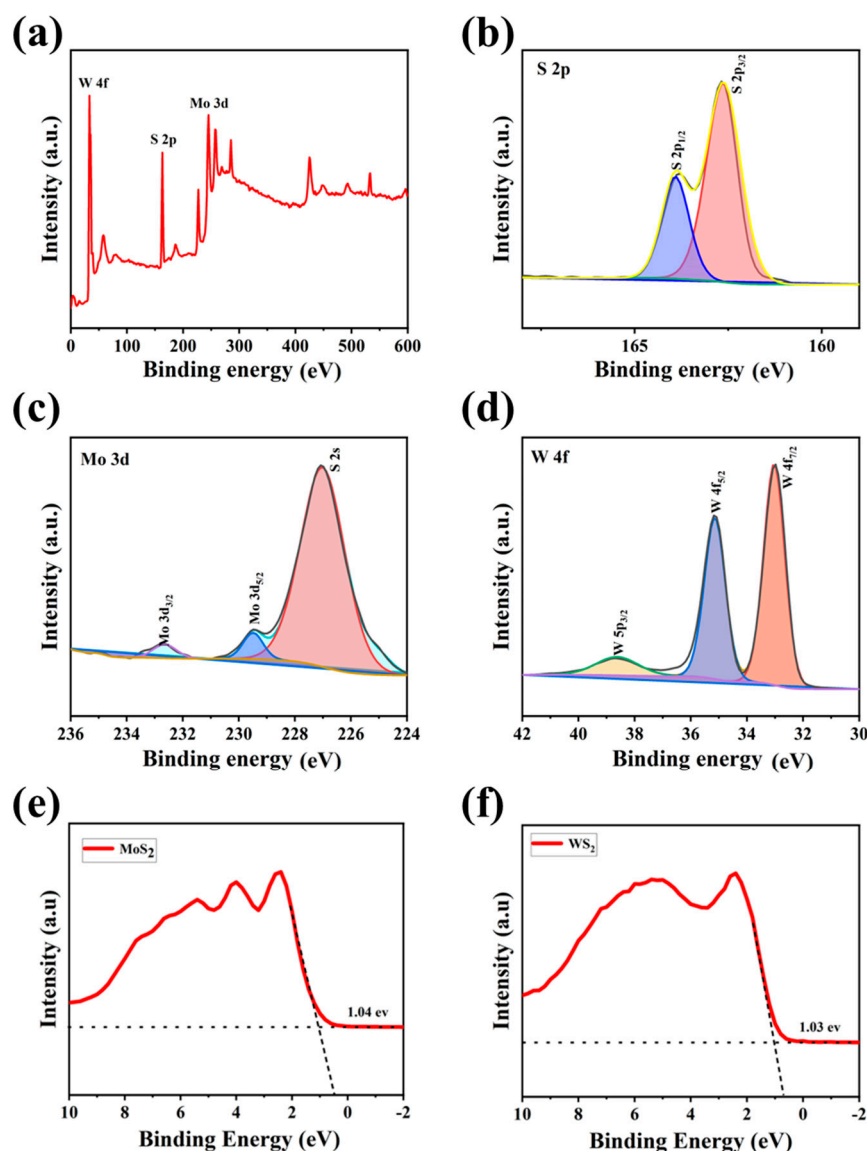


Figure 3. The XPS spectra of the 5 MW sample: (a) the survey spectrum, (b) high-resolution S 2p, (c) high-resolution Mo 3d, (d) high-resolution W 4f of the 5 MW sample, and (e,f) the VB-XPS spectra of MoS₂ and WS₂.

In order to determine the valence band positions of MoS₂ and WS₂, first we assessed the Mott-Schottky curves of the materials to determine the positions of the Fermi energy levels, and the energies between the valence bands to the Fermi energy levels were determined by VB-XPS [38]. The XPS valence band scan depicted in Figure 3e,f revealed that the energy gaps between the maximum valence band (VBM) and the Fermi energy levels are 1.04 eV for MoS₂ and 1.03 eV for WS₂, respectively. The dashed lines in Figures e,f are background fit lines of VB-XPS, which is to obtain the energy between valence band and the Fermi level.

SEM images of WS₂ in Figure 4a,b display a flake morphology with a thick and aggregated structure containing several grains attached to the surface. Figure 4c,d demonstrates that compared to the WS₂ samples, MoS₂ samples were less agglomerated and exhibited a flower-like morphology. Figure 4e–g displays the surface morphology of the 5 MW composite at different magnifications; the flower-like morphology can be observed more clearly in Figure 4g. Under high magnification SEM, the composite material displayed a lamellar structure. Figure 4f reveals that the 5 MW composite with a more uniform distribution exhibited a multilayer structure similar to that of the WS₂ flakes, thereby providing more

active sites for the desired gas absorption [39]. Figure 4h–j depicts the elemental mapping of the 5 MW composite, with a selected area shown in Figure 4g. In the 5 MW composites, S, Mo, and W were uniformly distributed, and no other elements were found.

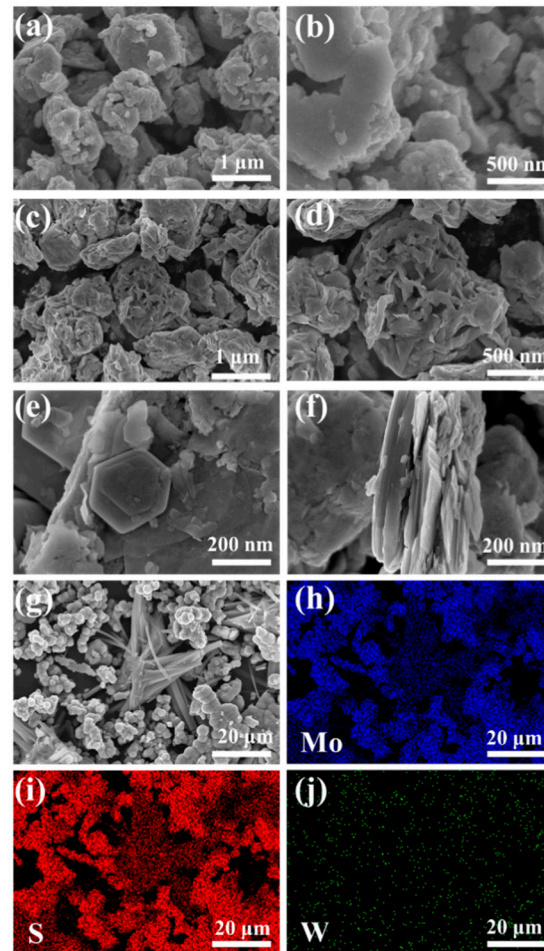


Figure 4. The SEM images of (a,b) WS₂. (c,d) MoS₂, and (e–g) 5 MW. (h–j) The elemental mapping of the 5 MW sample.

The formation of MoS₂/WS₂ heterogeneous structures was confirmed using TEM. Figure 5a,b displays the 5 MW composite with a distinct ductile laminate structure. Figure 5c reveals a low-magnification TEM image of the heterostructure, where the light contrast outer layer was MoS₂, while the inner layer was WS₂. In addition, the magnified TEM image in Figure 5d depicts the interface between WS₂ and MoS₂, in which G, H, I are selected regions to progress further HRTEM analysis. Figure 5e,f represent the fast Fourier transform (FFT) patterns generated from the MoS₂ and WS₂, respectively (regions G and H in Figure 5). The same orientation and alignment of these diffraction points indicate an epitaxial relationship existing between MoS₂ and WS₂. However, the thickness of the MoS₂ varies with the amount of MoS₂ precursors utilized during the synthesis. HRTEM images of Figure 5g–i corresponds to the region depicted in the (G,H,I) region of Figure 5d, where uniform lattices with a spacing of 0.174 nm and 0.282 nm are observed, corresponding to the (100) and (010) planes of MoS₂. The dotted stripe of 0.612 nm corresponds to the WS₂ (002) plane (Figure 5e). The clear interface observed between WS₂ and MoS₂ in Figure 5d indicates a semiconductor heterojunction structure formation. The semiconductor heterojunction structure improves the electron-hole separation and transport properties, thereby enhancing the response speed of the gas sensors [40].

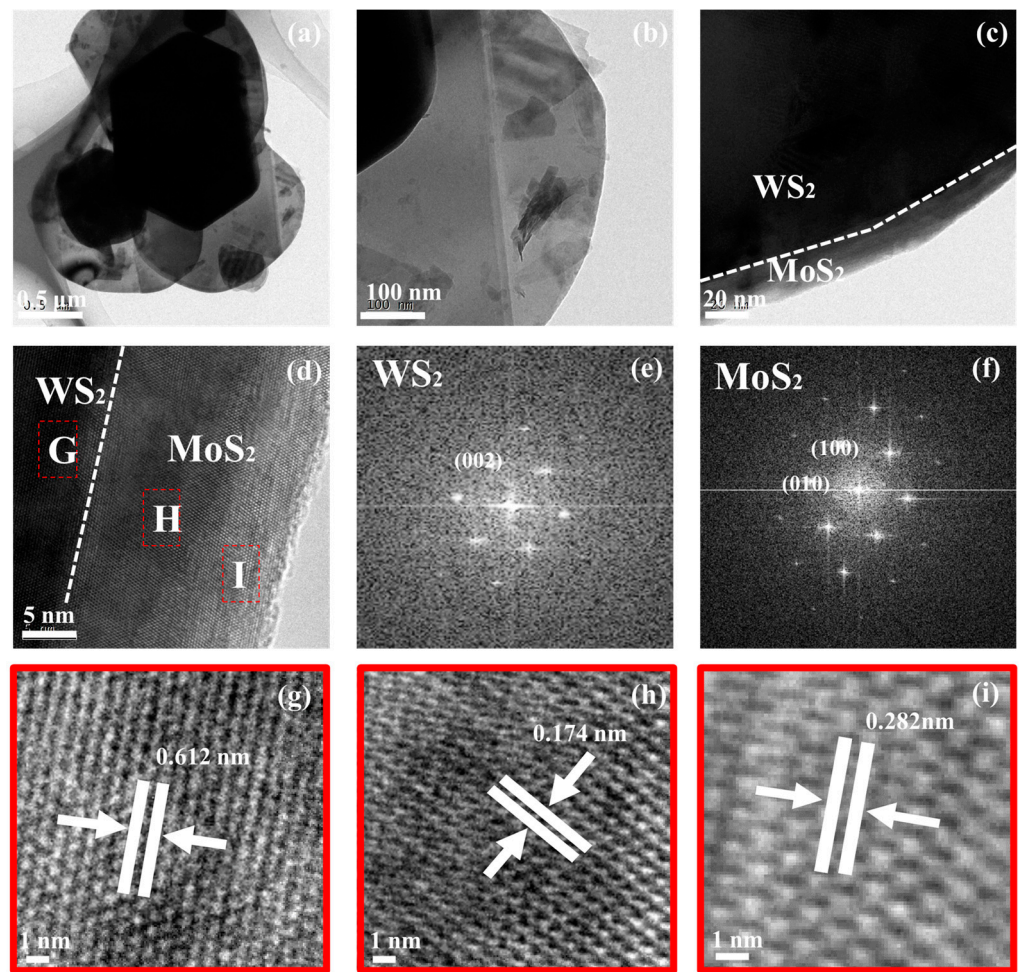


Figure 5. TEM images (a–d) and HRTEM images (g–i) of the 5 MW nanosheets; (e,f) are the FFT diffraction patterns of the dashed boxes (G,H region in (d)), which corresponds to the MoS₂ and WS₂ components, respectively.

The UV-Vis absorption spectra and Tauc plots of the WS₂, MoS₂, 3 MW, 5 MW, and 7 MW samples are depicted in Figure 6a–d. The MoS₂ and 3 MW, 5 MW, and 7 MW samples jumped at 320 nm due to the inhomogeneous surface of MoS₂, but this effect is very weak for the material forbidden band width. The composite samples exhibited strong light absorption near 310–600 nm in the visible and ultraviolet spectra. It is evident that increasing the MoS₂ content improves the absorption of the 3 MW, 5 MW, and 7 MW samples in the 400–760 nm range. Furthermore, the absorption edge of WS₂ shifted to the visible region (500–700 nm) after modification by MoS₂, which may be caused by the coupling band between WS₂ and MoS₂ and leads to a reduction in the exciton recombination time [41]. Figure 6b,d demonstrate the energy band gaps for the samples; the energy band gap E_g was calculated using the well-known Tauc plot. The calculation is performed as follows [42]:

$$(\alpha hv)^{1/n} = A(hv - E_g)$$

$$\alpha = 4\pi k/\lambda$$

where hv , α , k , and λ represent the photoelectron energy, absorption coefficient, absorption index, and wavelength of the photon, respectively, while n denotes the semiconductor type. In this work, the indirect transition was allowed [43]; therefore, $n = 2$. The calculated bandgaps of MoS₂ and WS₂ were 1.32 and 1.39 eV, respectively. It can also be determined according to the absorption edge, which was consistent with the bandgap calculated

through the tangent. The bandgap of MoS₂/WS₂ composites became narrower as the MoS₂ content increased, which facilitates the excitation of electrons from the valence band to the conduction band.

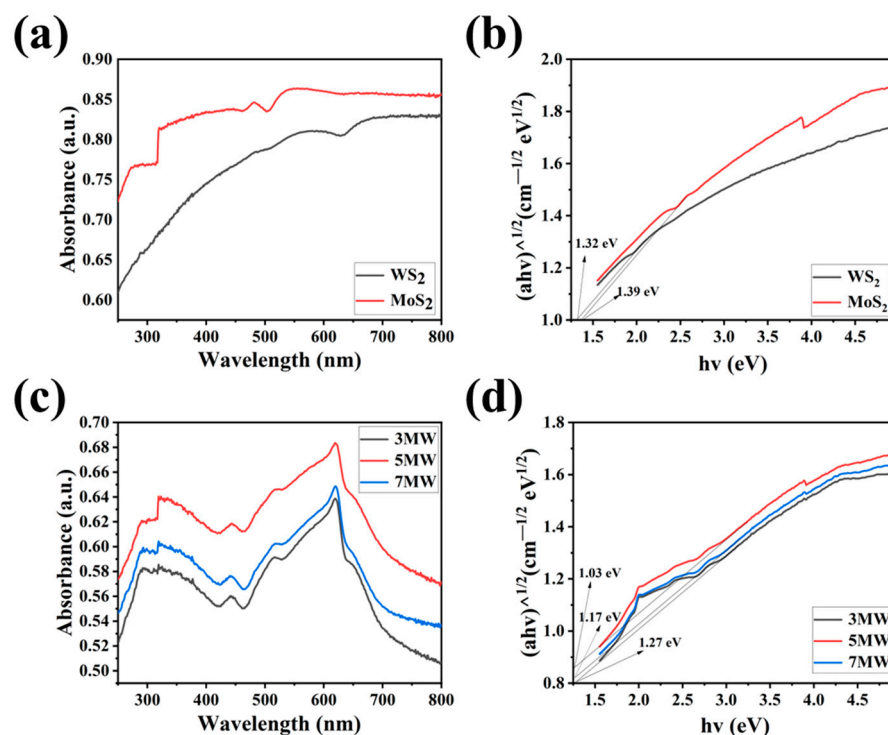


Figure 6. (a,c) The UV-Vis absorption spectra of the WS₂, MoS₂, 3 MW, 5 MW, and 7 MW samples. (b,d) Tauc plots showing the band gaps of the WS₂, MoS₂, 3 MW, 5 MW, and 7 MW samples.

The capacitance–voltage (C–V) relationship curves of the samples were measured with an electrochemical workstation (CHI-660E). The Mott-Schottky (M–S) curve was plotted with C^{-2} as the vertical axis and swept voltage as the horizontal axis. The slope of the most extended straight-line part of the curve determines the type of conductivity of the semiconductor [44]. Figure 7 depicts the Mott-Schottky curves for the pure-phase WS₂, MoS₂, and MoS₂/WS₂ composite solid powder samples. The Mott-Schottky slopes for the WS₂ and MoS₂ samples were positive, indicating that they are n-type semiconductors. The flat-band potentials (Fermi energy levels) were determined to be -0.16 V and -0.12 V, respectively (vs. NHE, pH = 7), by extending the linear part of the Mott-Schottky curve to the potential axis. The Mott-Schottky slope was also found to be positive in the MoS₂/WS₂ composite, indicating that it is an n-type semiconductor, and the flat-band potential (Fermi energy level) was -0.02 V (vs. NHE, pH = 7). An n–n heterojunction at the MoS₂ and WS₂ contact interface was confirmed using TEM analysis. This is consistent with the measurement results of the gas-sensing properties. When the VB-XPS result was combined with the Fermi energy levels of -0.16 V and -0.12 V, determined by Mott-Schottky analysis, the valence band positions for MoS₂ and WS₂ were calculated to be 0.88 V and 0.91 V, respectively. According to the UV-Vis absorption spectra, the band gap of WS₂ was 1.39 eV, and that of MoS₂ was 1.32 eV, respectively. The conduction bands of MoS₂ and WS₂ were located at -0.44 V and -0.48 V, respectively.

FT-IR spectral analysis reveals the surface chemical information and the vibrational modes of the chemical bonds present in the samples. Figure 8a–e depicts the IR spectra of MoS₂, WS₂, and their composite samples with varying relative mass ratios, revealing the surface functional groups. For WS₂, the stretching vibrations of the W–S bond peak were located at approximately 2950 and 582 cm^{-1} , respectively. Additionally, the S–S bond was at 1051 and 876 cm^{-1} , respectively [45,46]. MoS₂ exhibited typical Mo–S bond vibrations, with an absorption peak at 465 cm^{-1} [47]. The H–O–H bending motion and the O–H stretching

vibrations of the adsorbed water on the surface of the composite were reflected at the peaks of 1626 and 3430 cm^{-1} , respectively [48,49]. The broad peak at 3430 cm^{-1} was attributed to the symmetric and asymmetric O-H bond stretching patterns, which was more obvious in the composite material compared to the pure phases of WS_2 and MoS_2 . This is advantageous for the detection of NH_3 , as the hydroxyl group has gas adsorption capacity, and improves the selectivity in the detection of NH_3 due to the hydroxyl group's ability to hydrogen bond and weakly interact with ammonia, where the hydrogen molecules of ammonia combine with the oxygen molecules on the hydroxyl group to form a new chemical bond, thus allowing the ammonia to stay on the surface of the material for a longer period of time, which in turn improves the response of the material to NH_3 [50]. The peaks of the W-S, S-S, Mo-S, O-H, and H-O-H bonds in MoS_2/WS_2 composites were derived from the MoS_2 and WS_2 components. Furthermore, the slight variation in the spectral shape (Figure 8c–e) indicates that the same groups were observed in different composite samples. The increased number of hydroxyl groups indicates that the composites possess better NH_3 sensitivity properties than the pure phase.

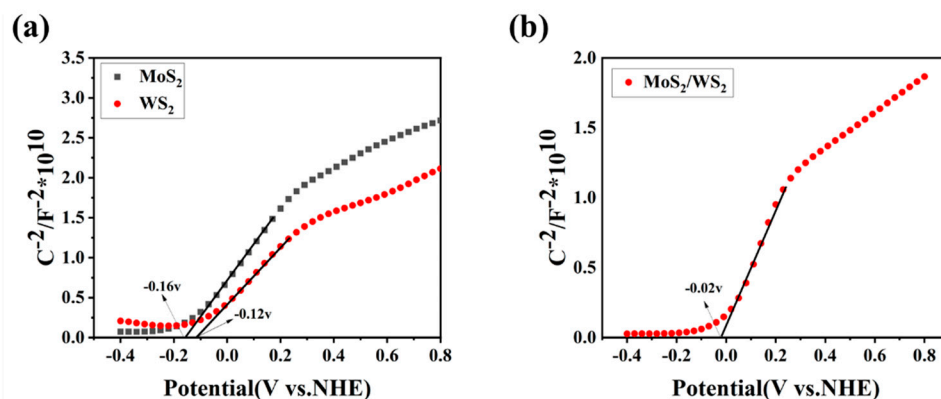


Figure 7. (a,b) The Mott-Schottky curves for the MoS_2 , WS_2 , and 5 MW samples.

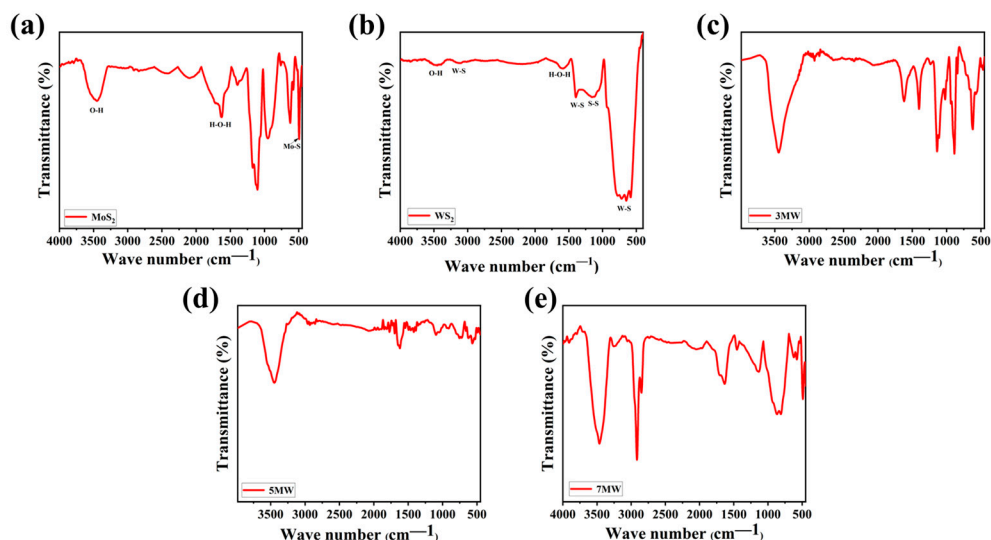


Figure 8. The FT-IR spectra of the (a) MoS_2 , (b) WS_2 , (c) 3 MW, (d) 5 MW, (e) 7 MW samples.

The dynamic responses of the WS_2 , MoS_2 , and MoS_2/WS_2 composites to formaldehyde (HCHO), ethanol ($\text{C}_2\text{H}_6\text{O}$), ammonia (NH_3), acetone ($\text{C}_3\text{H}_6\text{O}$), and hydrogen peroxide (H_2O_2) at room temperature are illustrated in Figure 9. The baseline current corresponds to an ambient test curve at approximately 30% RH (relative air humidity). The gas-sensing properties were obtained after three complete testing cycles, with the concentrations of all gases having been set to 500 ppm. Figure 9 demonstrates that the current response of the

gas sensor increased rapidly when exposed to the vapors of HCHO, C₂H₆O, NH₃, C₃H₆O, and H₂O₂. The response time is the time required to reach 90% of the maximum response current when the sensor is placed in the target gas, whereas the recovery is defined as the period of time when the sensor current changes to 10% of the response after removing the target gas. The response recovery curve in the figure reflects the n-type semiconductor's characteristics. In our tests we found that MoS₂ sometimes shows a negative response. This is because MoS₂ is an n-type semiconductor, which is inevitably disturbed by ambient humidity during the performance test, and the adsorption of water molecules on the MoS₂ surface equates to a p-type doping. As a result, the electrical properties change accordingly, and thus these samples show a response similar to the p-type semiconductor-based gas sensor in the reducing gas [51]. The responses of the pristine MoS₂ and WS₂-based sensors to NH₃ were approximately 320% and 90%, respectively; while both WS₂ and MoS₂ exhibited a low NH₃ response. The performance of composite-based sensors to HCHO, C₂H₆O, NH₃, and C₃H₆O was also investigated at room temperature. The 5 MW samples outperformed WS₂ and MoS₂ in terms of detection performance to 500 ppm NH₃ at a test voltage of 1 V, with a response of 23643%, enhanced by two orders of magnitude. Additionally, the 5 MW samples exhibited 2200%, 2310%, 672%, and 120% responses for other gases such as H₂O₂, C₃H₆O, HCHO, and C₂H₆O, respectively, indicating a good selectivity for the detection of targeted NH₃ gases. The recovery time of the composite samples was particularly fast, with a relatively long response time for the detection of these five gases. The 5 MW composite exhibited a response time of 30 s and a recovery time of 2.6 s. The 5 MW samples demonstrated a good reproducibility for NH₃ detection after consecutive test cycles. These results reveal that the prepared 5 MW samples are excellent for NH₃ detection at room temperature, and that the introduction of composite components improves the gas-sensing properties of pristine WS₂ or MoS₂ samples.

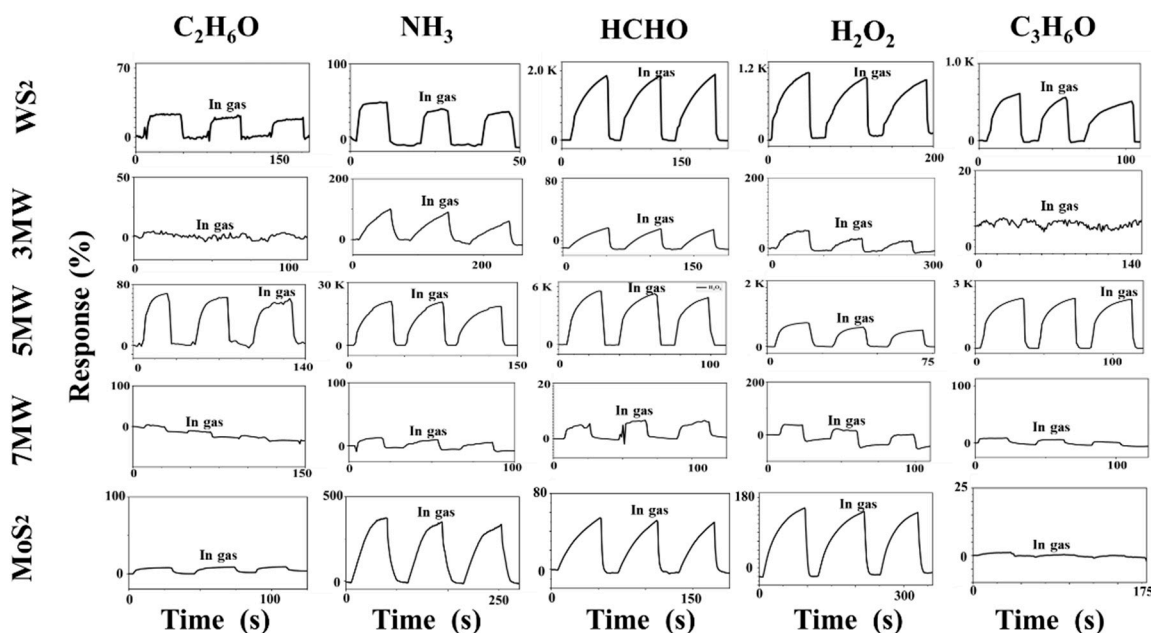


Figure 9. Responses of MoS₂, WS₂, and their composites to different gases (C₂H₆O, NH₃, HCHO, H₂O₂, and C₃H₆O, respectively) of 500 ppm, 30% RH at room temperature.

The selectivity plots of WS₂, MoS₂ and MoS₂/WS₂ composites for HCHO, C₂H₆O, NH₃, C₃H₆O, and H₂O₂ gases are depicted in Figure 10a. When compared to other composite samples, the response of the 5 MW sample to NH₃ reached nearly four orders of magnitude higher, demonstrating that the 5 MW samples exhibit a high selectivity for NH₃ detection. The histogram of response/recovery time is shown in Figure 10b. Compared with other samples, the 5 MW composite had a response time of about 30 s and a recovery

time of only 2.6 s, revealing an efficient detection performance and a fast recovery for NH₃ detection. Figure 10c,d depicts the response versus different concentrations of NH₃ at room temperature. The current response of the 5 MW gas sensor increases with increasing NH₃ concentration, which can be attributed to the increased possibility of gas adsorption at the active sites on the sample surface. In addition, the 5 MW gas sensor exhibits a highly linear relationship for NH₃ detection in the concentration range of 20–500 ppm. The linear relation was as follows: $R = 0.39287C + 15.60856$ ($R^2 = 0.98137$ in Figure 10e). Figure 10f exhibits a six-month response comparison of the 5 MW sensor to 500 ppm NH₃ at room temperature. The response reaches four orders of magnitude both before and after six months, confirming the excellent long-term stability of the 5 MW gas sensor.

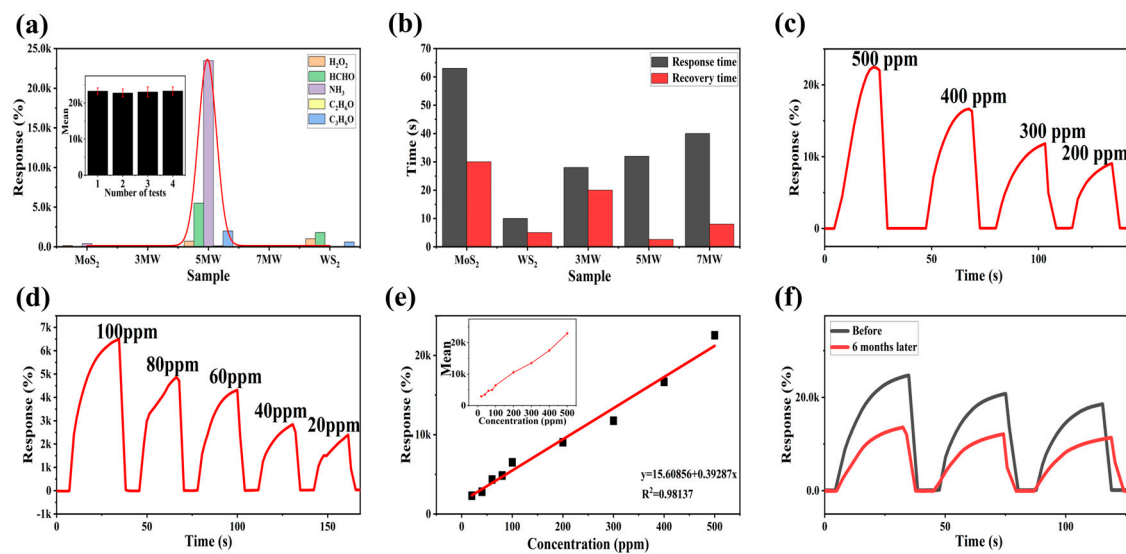


Figure 10. (a) Selectivity of MoS₂, WS₂, and composite samples for different gases of 500 ppm at room temperature. (b) Response and recovery time of the 5 MW-based gas sensor to 500 ppm NH₃ at room temperature. (c,d) Responses of the 5 MW sample to different concentrations of NH₃ at room temperature. (e) Linear response of the 5 MW sensor to varying concentrations of NH₃. (f) Long-term stability of the 5 MW sensor for six months.

Humidity immunity tests were performed to eliminate humidity interference with the gas sensor. The prepared sensors were placed in chambers with different humidity levels (11–95% RH) by rapidly switching the sensors from one chamber to another. Impedance versus humidity curves for the pristine MoS₂ and WS₂ at 100 Hz, AC 1 V are displayed in Figure 11a. The response was less than one order of magnitude for MoS₂ and one order of magnitude for WS₂ over the humidity range of 11–95% RH. Figure 11b reveals that the 5 MW composite exhibited excellent humidity immunity, and the moisture-sensitive response was less than an order of magnitude. These results indicate that both the pure-phase and composite samples had a high humidity resistance.

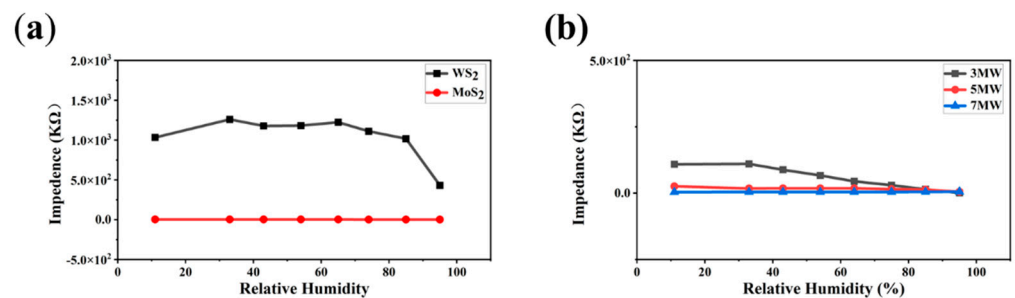


Figure 11. (a) Response curves of the MoS₂, WS₂ samples to 11–95% RH; (b) Response curves of the MoS₂/WS₂ composites to 11–95% RH.

Table 1 summarizes the performance of NH₃ sensors reported in the literature in recent years. Compared to the previous studies, the 5 MW composite prepared in this work exhibits a shorter recovery time (2.6 s), and a higher response of 23643% to 500 ppm NH₃.

Table 1. Comparison of sensing parameters of the 5 MW sensor with previously reported sensors.

Materials	T (°C)	Concentration (ppm)	Response/Recovery Time (s)	Limit of Detection (ppm)	Gas Type	Response	Ref.
P-MoS ₂	150 °C	50	1300/1250	10	NH ₃	651.53%	[52]
Ti ₃ C ₂ Tx	RT	100	-	9.27	NH ₃	21%	[53]
C-xy graphene	RT	500	-	-	NH ₃	4200%	[54]
Pt-Ti ₃ C ₂ Tx/TiO ₂	RT	100	23/24	10	NH ₃	45.5%	[55]
Ti ₃ C ₂ Tx/Ti ₃ AlC ₂	RT	0.5	90/75	0.05	NH ₃	1.2%	[56]
MoS ₂ /WS ₂	RT	500	30/2.6	20	NH ₃	23643%	This work

4. Discussion

The energy band was determined by combining the Mott-Schottky curve, XPS valence band spectrum, and UV-visible absorption spectrum, as illustrated in Figure 12. As demonstrated through the previous analysis, the slopes of Mott-Schottky curves of WS₂, MoS₂ and MoS₂/WS₂ samples were all positive, implying that the prepared samples are n-type semiconductors, while the TEM analysis demonstrated that heterostructures were formed between the two components. In particular, n-n-type MoS₂/WS₂ heterostructures were developed in this study, which are commensurate with the adsorption–desorption curve characteristics of WS₂, MoS₂, and MoS₂/WS₂ sensors. The electrons would be transferred between MoS₂ and WS₂ until the Fermi energy level reaches equilibrium.

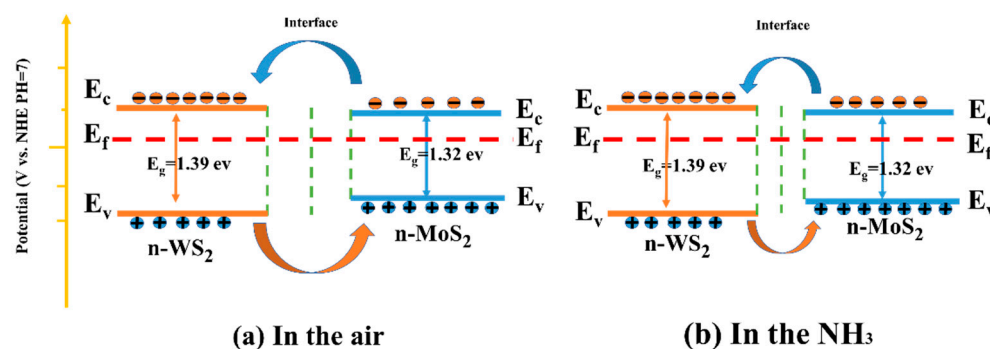


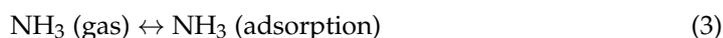
Figure 12. The sensing mechanism of the MoS₂/WS₂ gas sensor in (a) air and (b) NH₃.

The NH₃ gas-sensitive mechanism of the MoS₂/WS₂ sensor was explained using a surface resistance control model, which included the change in the sensor resistance due to the redox reaction between the chemisorbed oxygen and the target gas molecules [57]. When the MoS₂/WS₂ composite was exposed to air at room temperature, O₂ molecules were adsorbed on the sample surface, and free electrons on the composite surface were captured by O₂ to produce surface adsorbed species (O²⁻, O⁻, O₂⁻), as illustrated in Figure 12a. The corresponding reaction processes are described in Equations (1) and (2) [58].



At this point, a wide depletion layer has been formed on the sample surface due to a severe lack of electrons, while the sensor's resistance is high. When the MoS₂/WS₂

composite is exposed to NH_3 , the reducing gas interacts with the adsorbed O_2^- to produce H_2O , N_2 , and free electrons, according to Equations (3) and (4).



The captured electrons are subsequently returned to the sample surface. This process significantly reduces the thickness of the electron depletion layer. As a result, the electron depletion layer narrows, and the resistance reduces (Figure 12b).

The development of the heterojunction was deemed to be the main reason for the enhanced gas-sensitive response. As previously demonstrated, WS_2 and MoS_2 are n-type semiconductors with electrons as the main charge carriers. The Fermi energy level of MoS_2 was higher than that of WS_2 , as illustrated by the Mott-Schottky curves. Electrons would be transported in the air from MoS_2 to WS_2 until the Fermi energy levels reached equilibrium. In contrast, carriers (holes) leaving the valence band would diffuse in the opposite direction to achieve effective charge-carrier separation. Consequently, the energy band bends, creating a barrier that impedes electron transport. Therefore, the baseline resistance of the WS_2/MoS_2 sensors significantly increased. The resistance was further reduced when the sensor was placed in NH_3 since the electrons released by the reaction with O_2^- lowered the potential barrier in the heterojunction region. Therefore, the sensing performance of MoS_2/WS_2 composites to NH_3 was enhanced due to the substantial change in device resistance [59,60].

On the other hand, the superior sensing performance of the MoS_2/WS_2 composites over pristine WS_2 and MoS_2 can be attributed to the flower-like morphology of the WS_2/MoS_2 composites compared to the homogeneous sheet-like morphology of pure-phase WS_2 and MoS_2 , which provides more active sites for surface reactions and promotes gas adsorption and desorption, thus improving the gas-sensing response.

In short, the excellent gas-sensing properties of MoS_2/WS_2 composites are attributed to the gain effect of the n-n heterojunction and unique surface morphology.

5. Conclusions

In this study, MoS_2/WS_2 composites were prepared using a one-step hydrothermal method that is highly adaptable, affordable, and accessible. A heterostructure was successfully formed by controlling the relative mass ratio of WS_2 and MoS_2 , revealing carrier movement and transformation at the MoS_2/WS_2 interface. The positions of the valence and conduction bands of the two-component semiconductors were determined by the Mott-Schottky curves, UV-Vis spectra, and XPS valence band spectra. Afterward, $\text{WS}_2\text{-MoS}_2$ heterojunction-based gas-sensitive sensors were fabricated. The 5 MW sample exhibited good gas-sensitive characteristics when the relative mass ratio of MoS_2 and WS_2 was 50 wt% with a response of 23643% for 500 ppm NH_3 gas, a fast recovery time of 2.6 s, a detection limit of 20 ppm, and long-term stability for six months. The humidity immune test demonstrated that the 5 MW sample possesses good moisture resistance in the humidity range of 11–95% RH. This work provides an approach for the simple and low-cost preparation of two-dimensional gas-sensing materials with heterostructures. It also provides a facile way to obtain NH_3 gas sensors working at room temperature.

Author Contributions: M.Z. and J.Z. conceived and designed the experiments, J.Z. performed the experiments, M.Z. and J.Z. analyzed the data and wrote the paper. All authors have read and agreed to the published version of the manuscript.

Funding: This research was funded by the National Natural Science Foundation of China (Grant Nos. 22262033), and the Natural Science Foundation of Xinjiang Uygur Autonomous Region (2021D01C031).

Data Availability Statement: The data presented in this study are available on request from the corresponding author.

Conflicts of Interest: The authors declare no conflict of interest.

References

1. Krupa, S.V. Effects of atmospheric ammonia (NH₃) on terrestrial vegetation: A review. *Environ. Pollut.* **2003**, *124*, 179–221. [[CrossRef](#)] [[PubMed](#)]
2. Boron, W.F.; De Weer, P. Intracellular pH transients in squid giant axons caused by CO₂, NH₃, and metabolic inhibitors. *J. Gen. Physiol.* **1976**, *67*, 91–112. [[CrossRef](#)] [[PubMed](#)]
3. Li, J.; Chang, H.; Ma, L.; Hao, J.; Yang, R.T. Low-temperature selective catalytic reduction of NO_x with NH₃ over metal oxide and zeolite catalysts—A review. *Catal. Today* **2011**, *175*, 147–156. [[CrossRef](#)]
4. Sufriadi, E.; Meilina, H.; Munawar, A.A.; Muhammad, S.; Idroes, R. Identification of β-Caryophyllene (BCP) in Aceh Patchouli Essential Oil (PEO) using Gas Chromatography-Mass Spectrometry (GC-MS), IOP Conference Series: Earth and Environmental Science, 2021; IOP Publishing: Bristol, UK, 2021; p. 12032.
5. Bartle, K.D.; Myers, P. History of gas chromatography. *TrAC Trends Anal. Chem.* **2002**, *21*, 547–557. [[CrossRef](#)]
6. Bakker, E.; Telting-Diaz, M. Electrochemical sensors. *Anal. Chem.* **2002**, *74*, 2781–2800. [[CrossRef](#)]
7. Fine, G.F.; Cavanagh, L.M.; Afonja, A.; Binions, R. Metal oxide semi-conductor gas sensors in environmental monitoring. *Sensors-Basel* **2010**, *10*, 5469–5502. [[CrossRef](#)]
8. Nikolic, M.V.; Milovanovic, V.; Vasiljevic, Z.Z.; Stamenkovic, Z. Semiconductor gas sensors: Materials, technology, design, and application. *Sensors* **2020**, *20*, 6694. [[CrossRef](#)]
9. Gu, J.; Chakraborty, B.; Khatoniar, M.; Menon, V.M. A room-temperature polariton light-emitting diode based on monolayer WS₂. *Nat. Nanotechnol.* **2019**, *14*, 1024–1028. [[CrossRef](#)]
10. Kim, J.; Mirzaei, A.; Kim, H.W.; Kim, S.S. Realization of Au-decorated WS₂ nanosheets as low power-consumption and selective gas sensors. *Sens. Actuators B Chem.* **2019**, *296*, 126659. [[CrossRef](#)]
11. Sharma, S.; Saini, R.; Gupta, G.; Late, D.J. Room-temperature highly sensitive and selective NH₃ gas sensor using vertically aligned WS₂ nanosheets. *Nanotechnology* **2022**, *34*, 45704. [[CrossRef](#)]
12. Xu, P.; Cheng, Z.; Pan, Q.; Xu, J.; Xiang, Q.; Yu, W.; Chu, Y. High aspect ratio In₂O₃ nanowires: Synthesis, mechanism and NO₂ gas-sensing properties. *Sens. Actuators B Chem.* **2008**, *130*, 802–808. [[CrossRef](#)]
13. Qin, Z.; Song, X.; Wang, J.; Li, X.; Wu, C.; Wang, X.; Yin, X.; Zeng, D. Development of flexible paper substrate sensor based on 2D WS₂ with S defects for room-temperature NH₃ gas sensing. *Appl. Surf. Sci.* **2022**, *573*, 151535. [[CrossRef](#)]
14. Yu, S.M.; Kim, J.H.; Yoon, K.R.; Jung, J.W.; Oh, J.H.; Kim, I.D. *Single Layers of WS₂ Nanoplates Anchored to Hollow N-Doped Carbon Nanofibers as Efficient Electrocatalysts for Hydrogen Evolution*, 2015 Fall MRS, 2015; Materials Research Society: Warrendale, PA, USA, 2015.
15. Zhao, F.; Li, Z.; Fu, Y.; Wang, Q. Gas-Sensitive Characteristics of Graphene Composite Tungsten Disulfide to Ammonia. *Sensors* **2022**, *22*, 8672. [[CrossRef](#)] [[PubMed](#)]
16. Järvinen, T.; Lorite, G.S.; Peräntie, J.; Toth, G.; Saarakkala, S.; Virtanen, V.K.; Kordas, K. WS₂ and MoS₂ thin film gas sensors with high response to NH₃ in air at low temperature. *Nanotechnology* **2019**, *30*, 405501. [[CrossRef](#)] [[PubMed](#)]
17. Late, D.J.; Kanawade, R.V.; Kannan, P.K.; Rout, C.S. Atomically thin WS₂ nanosheets based gas sensor. *Sens. Lett.* **2016**, *14*, 1249–1254. [[CrossRef](#)]
18. Perrozzi, F.; Emamjomeh, S.M.; Paolucci, V.; Taglieri, G.; Ottaviano, L.; Cantalini, C. Thermal stability of WS₂ flakes and gas sensing properties of WS₂/WO₃ composite to H₂, NH₃ and NO₂. *Sens. Actuators B Chem.* **2017**, *243*, 812–822. [[CrossRef](#)]
19. Luo, H.; Shi, J.; Liu, C.; Chen, X.; Lv, W.; Zhou, Y.; Zeng, M.; Yang, J.; Wei, H.; Zhou, Z. Design of p-p heterojunctions based on CuO decorated WS₂ nanosheets for sensitive NH₃ gas sensing at room temperature. *Nanotechnology* **2021**, *32*, 445502. [[CrossRef](#)]
20. Ouyang, C.; Chen, Y.; Qin, Z.; Zeng, D.; Zhang, J.; Wang, H.; Xie, C. Two-dimensional WS₂-based nanosheets modified by Pt quantum dots for enhanced room-temperature NH₃ sensing properties. *Appl. Surf. Sci.* **2018**, *455*, 45–52. [[CrossRef](#)]
21. Singh, S.; Saggi, I.S.; Chen, K.; Xuan, Z.; Swihart, M.T.; Sharma, S. Humidity-tolerant room-temperature selective dual sensing and discrimination of NH₃ and NO₂ using a WS₂/MWCNT Composite. *ACS Appl. Mater. Inter.* **2022**, *14*, 40382–40395. [[CrossRef](#)]
22. Paolucci, V.; Emamjomeh, S.M.; Ottaviano, L.; Cantalini, C. Near room temperature light-activated WS₂-decorated rGO as NO₂ gas sensor. *Sensors* **2019**, *19*, 2617. [[CrossRef](#)]
23. Yadav, A.A.; Hunge, Y.M.; Kang, S. Visible Light-Responsive CeO₂/MoS₂ Composite for Photocatalytic Hydrogen Production. *Catalysts* **2022**, *12*, 1185. [[CrossRef](#)]
24. Hunge, Y.M.; Yadav, A.A.; Kang, S.; Lim, S.J.; Kim, H. Visible light activated MoS₂/ZnO composites for photocatalytic degradation of ciprofloxacin antibiotic and hydrogen production. *J. Photochem. Photobiol. A Chem.* **2023**, *434*, 114250. [[CrossRef](#)]
25. Hunge, Y.M.; Yadav, A.A.; Kang, S. Photocatalytic Degradation of Eriochrome Black-T Using BaWO₄/MoS₂ Composite. *Catalysts* **2022**, *12*, 1290. [[CrossRef](#)]
26. Zhang, J.; Wang, J.; Chen, P.; Sun, Y.; Wu, S.; Jia, Z.; Lu, X.; Yu, H.; Chen, W.; Zhu, J. Observation of strong interlayer coupling in MoS₂/WS₂ heterostructures. *Adv. Mater.* **2016**, *28*, 1950–1956. [[CrossRef](#)] [[PubMed](#)]

27. Vikraman, D.; Hussain, S.; Akbar, K.; Truong, L.; Kathalingam, A.; Chun, S.; Jung, J.; Park, H.J.; Kim, H. Improved hydrogen evolution reaction performance using MoS₂-WS₂ heterostructures by physicochemical process. *ACS Sustain. Chem. Eng.* **2018**, *6*, 8400–8409. [[CrossRef](#)]
28. Yu, Y.; Hu, S.; Su, L.; Huang, L.; Liu, Y.; Jin, Z.; Purezky, A.A.; Geohegan, D.B.; Kim, K.W.; Zhang, Y. Equally efficient interlayer exciton relaxation and improved absorption in epitaxial and nonepitaxial MoS₂/WS₂ heterostructures. *Nano Lett.* **2015**, *15*, 486–491. [[CrossRef](#)] [[PubMed](#)]
29. Chen, H.; Wen, X.; Zhang, J.; Wu, T.; Gong, Y.; Zhang, X.; Yuan, J.; Yi, C.; Lou, J.; Ajayan, P.M. Ultrafast formation of interlayer hot excitons in atomically thin MoS₂/WS₂ heterostructures. *Nat. Commun.* **2016**, *7*, 12512. [[CrossRef](#)]
30. Chen, S.; Pan, Y. Enhancing catalytic properties of noble metal@ MoS₂/WS₂ heterojunction for the hydrogen evolution reaction. *Appl. Surf. Sci.* **2022**, *591*, 153168. [[CrossRef](#)]
31. Deilmann, T.; Thygesen, K.S. Interlayer triions in the MoS₂/WS₂ van der Waals heterostructure. *Nano Lett.* **2018**, *18*, 1460–1465. [[CrossRef](#)]
32. Kaushik, V.; Ahmad, M.; Agarwal, K.; Varandani, D.; Belle, B.D.; Das, P.; Mehta, B.R. Charge transport in 2D MoS₂, WS₂, and MoS₂-WS₂ heterojunction-based field-effect transistors: Role of bipolarity. *J. Phys. Chem. C* **2020**, *124*, 23368–23379. [[CrossRef](#)]
33. Chiappe, D.; Asselberghs, I.; Sutar, S.; Iacovo, S.; Afanas' Ev, V.; Stesmans, A.; Balaji, Y.; Peters, L.; Heyne, M.; Mannarino, M. Controlled sulfurization process for the synthesis of large area MoS₂ films and MoS₂/WS₂ heterostructures. *Adv. Mater. Interfaces* **2016**, *3*, 1500635. [[CrossRef](#)]
34. Sharma, A.; Mahlouji, R.; Wu, L.; Verheijen, M.A.; Vandalon, V.; Balasubramanyam, S.; Hofmann, J.P.; Kessels, W.E.; Bol, A.A. Large area, patterned growth of 2D MoS₂ and lateral MoS₂-WS₂ heterostructures for nano-and opto-electronic applications. *Nanotechnology* **2020**, *31*, 255603. [[CrossRef](#)] [[PubMed](#)]
35. Hong, X.; Kim, J.; Shi, S.; Zhang, Y.; Jin, C.; Sun, Y.; Tongay, S.; Wu, J.; Zhang, Y.; Wang, F. Ultrafast charge transfer in atomically thin MoS₂/WS₂ heterostructures. *Nat Nanotechnol* **2014**, *9*, 682–686. [[CrossRef](#)] [[PubMed](#)]
36. Xiong, Y.F.; Chen, J.H.; Lu, Y.Q.; Xu, F. Broadband optical-fiber-compatible photodetector based on a graphene-MoS₂-WS₂ heterostructure with a synergetic photogenerating mechanism. *Adv. Electron. Mater.* **2019**, *5*, 1800562. [[CrossRef](#)]
37. Tang, M.; Zhang, D.; Wang, D.; Deng, J.; Kong, D.; Zhang, H. Performance prediction of 2D vertically stacked MoS₂-WS₂ heterostructures base on first-principles theory and Pearson correlation coefficient. *Appl. Surf. Sci.* **2022**, *596*, 153498. [[CrossRef](#)]
38. Zhao, X.; Tang, G.; Li, Y.; Zhang, M.; Nie, Y. Biaxial strain improving the thermoelectric performance of a two-dimensional MoS₂/WS₂ heterostructure. *ACS Appl. Electron. Ma* **2021**, *3*, 2995–3004. [[CrossRef](#)]
39. Zhang, X.; Huangfu, L.; Gu, Z.; Xiao, S.; Zhou, J.; Nan, H.; Gu, X.; Ostrikov, K. Controllable Epitaxial Growth of Large-Area MoS₂/WS₂ Vertical Heterostructures by Confined-Space Chemical Vapor Deposition. *Small* **2021**, *17*, 2007312. [[CrossRef](#)]
40. Choudhary, N.; Park, J.; Hwang, J.Y.; Chung, H.; Dumas, K.H.; Khondaker, S.I.; Choi, W.; Jung, Y. Centimeter scale patterned growth of vertically stacked few layer only 2D MoS₂/WS₂ van der Waals heterostructure. *Sci. Rep.* **2016**, *6*, 1–7. [[CrossRef](#)]
41. Pesci, F.M.; Sokolikova, M.S.; Grotta, C.; Sherrell, P.C.; Reale, F.; Sharda, K.; Ni, N.; Palczynski, P.; Mattevi, C. MoS₂/WS₂ heterojunction for photoelectrochemical water oxidation. *ACS Catal.* **2017**, *7*, 4990–4998. [[CrossRef](#)]
42. Wang, L.; Tahir, M.; Chen, H.; Sambur, J.B. Probing charge carrier transport and recombination pathways in monolayer MoS₂/WS₂ heterojunction photoelectrodes. *Nano Lett.* **2019**, *19*, 9084–9094. [[CrossRef](#)]
43. Lin, Z.; Luo, P.; Zeng, W.; Lai, H.; Xie, W.; Deng, W.; Luo, Z. Improvement of photoelectric properties of MoS₂/WS₂ heterostructure photodetector with interlayer of Au nanoparticles. *Opt. Mater.* **2020**, *108*, 110191. [[CrossRef](#)]
44. Zhang, X.; Xiao, S.; Nan, H.; Mo, H.; Wan, X.; Gu, X.; Ostrikov, K.K. Controllable one-step growth of bilayer MoS₂-WS₂/WS₂ heterostructures by chemical vapor deposition. *Nanotechnology* **2018**, *29*, 455707. [[CrossRef](#)] [[PubMed](#)]
45. Kang, J.; Sahin, H.; Peeters, F.M. Tuning carrier confinement in the MoS₂/WS₂ lateral heterostructure. *J. Phys. Chem. C* **2015**, *119*, 9580–9586. [[CrossRef](#)]
46. Xue, Y.; Zhang, Y.; Liu, Y.; Liu, H.; Song, J.; Sophia, J.; Liu, J.; Xu, Z.; Xu, Q.; Wang, Z. Scalable production of a few-layer MoS₂/WS₂ vertical heterojunction array and its application for photodetectors. *ACS Nano* **2016**, *10*, 573–580. [[CrossRef](#)]
47. Shan, J.; Li, J.; Chu, X.; Xu, M.; Jin, F.; Fang, X.; Wei, Z.; Wang, X. Enhanced photoresponse characteristics of transistors using CVD-grown MoS₂/WS₂ heterostructures. *Appl. Surf. Sci.* **2018**, *443*, 31–38. [[CrossRef](#)]
48. Zeng, Y.; Dai, W.; Ma, R.; Li, Z.; Ou, Z.; Wang, C.; Yu, Y.; Zhu, T.; Liu, X.; Wang, T. Distinguishing Ultrafast Energy Transfer in Atomically Thin MoS₂/WS₂ Heterostructures. *Small* **2022**, *18*, 2204317. [[CrossRef](#)]
49. Wang, F.; Wang, J.; Guo, S.; Zhang, J.; Hu, Z.; Chu, J. Tuning coupling behavior of stacked heterostructures based on MoS₂, WS₂, and WSe₂. *Sci. Rep.* **2017**, *7*, 1–10. [[CrossRef](#)]
50. Wang, J.; Li, Z.; Zhang, S.; Yan, S.; Cao, B.; Wang, Z.; Fu, Y. Enhanced NH₃ gas-sensing performance of silica modified CeO₂ nanostructure based sensors. *Sens. Actuators B Chem.* **2018**, *255*, 862–870. [[CrossRef](#)]
51. Zhao, J.; Li, N.; Yu, H.; Wei, Z.; Liao, M.; Chen, P.; Wang, S.; Shi, D.; Sun, Q.; Zhang, G. Highly sensitive MoS₂ humidity sensors array for noncontact sensation. *Adv. Mater.* **2017**, *29*, 1702076. [[CrossRef](#)]
52. Kim, T.; Lee, T.H.; Park, S.Y.; Eom, T.H.; Cho, I.; Kim, Y.; Kim, C.; Lee, S.A.; Choi, M.; Suh, J.M. Drastic Gas Sensing Selectivity in 2-Dimensional MoS₂ Nanoflakes by Noble Metal Decoration. *Acs Nano* **2023**, *17*, 4404–4413. [[CrossRef](#)]
53. Lee, E.; VahidMohammadi, A.; Prorok, B.C.; Yoon, Y.S.; Beidaghi, M.; Kim, D. Room temperature gas sensing of two-dimensional titanium carbide (MXene). *ACS Appl. Mater. Inter.* **2017**, *9*, 37184–37190. [[CrossRef](#)] [[PubMed](#)]

54. Rabchinskii, M.K.; Sysoev, V.V.; Glukhova, O.E.; Brzhezinskaya, M.; Stolyarova, D.Y.; Varezchnikov, A.S.; Solomatin, M.A.; Barkov, P.V.; Kirilenko, D.A.; Pavlov, S.I. Guiding Graphene Derivatization for the On-Chip Multisensor Arrays: From the Synthesis to the Theoretical Background. *Adv. Mater. Technol.* **2022**, *7*, 2101250. [[CrossRef](#)]
55. Zhang, H.; Wang, L.; Zou, Y.; Li, Y.; Xuan, J.; Wang, X.; Jia, F.; Yin, G.; Sun, M. Enhanced ammonia sensing response based on Pt-decorated $Ti_3C_2T_x/TiO_2$ composite at room temperature. *Nanotechnology* **2023**, *34*, 205501. [[CrossRef](#)]
56. Liu, Z.; Han, D.; Liu, L.; Li, D.; Han, X.; Chen, Y.; Liu, X.; Zhuo, K.; Cheng, Y.; Sang, S. Ultrasensitive ammonia gas sensor based on $Ti_3C_2T_x/Ti_3AlC_2$ planar composite at room temperature. *Sens. Actuators B Chem.* **2023**, *378*, 133149. [[CrossRef](#)]
57. Wang, L.; Meng, W.; He, Z.; Meng, W.; Li, Y.; Dai, L. Enhanced selective performance of mixed potential ammonia gas sensor by Au nanoparticles decorated $CeVO_4$ sensing electrode. *Sens. Actuators B Chem.* **2018**, *272*, 219–228. [[CrossRef](#)]
58. Rigosi, A.F.; Hill, H.M.; Li, Y.; Chernikov, A.; Heinz, T.F. Probing interlayer interactions in transition metal dichalcogenide heterostructures by optical spectroscopy: MoS_2/WS_2 and $MoSe_2/WSe_2$. *Nano Lett.* **2015**, *15*, 5033–5038. [[CrossRef](#)] [[PubMed](#)]
59. Bogaert, K.; Liu, S.; Chesin, J.; Titow, D.; Gradecak, S.; Garaj, S. Diffusion-mediated synthesis of MoS_2/WS_2 lateral heterostructures. *Nano Lett.* **2016**, *16*, 5129–5134. [[CrossRef](#)]
60. He, X.; Li, H.; Zhu, Z.; Dai, Z.; Yang, Y.; Yang, P.; Zhang, Q.; Li, P.; Schwingenschlogl, U.; Zhang, X. Strain engineering in monolayer WS_2 , MoS_2 , and the WS_2/MoS_2 heterostructure. *Appl. Phys. Lett.* **2016**, *109*, 173105. [[CrossRef](#)]

Disclaimer/Publisher's Note: The statements, opinions and data contained in all publications are solely those of the individual author(s) and contributor(s) and not of MDPI and/or the editor(s). MDPI and/or the editor(s) disclaim responsibility for any injury to people or property resulting from any ideas, methods, instructions or products referred to in the content.